THE RELATION BETWEEN COOL CLUSTER CORES AND *HERSCHEL*-DETECTED STAR FORMATION IN BRIGHTEST CLUSTER GALAXIES[*]

T. D. Rawle[1], A. C. Edge[2], E. Egami[1], M. Rex[1], G. P. Smith[3], B. Altieri[4], A. Fiedler[1], C. P. Haines[1,3], M. J. Pereira[1],
P. G. Pérez-González[5,9], J. Portouw[1], I. Valtchanov[4], G. Walth[1], P. P. van der Werf[6], and M. Zemcov[7,8]

[1] Steward Observatory, University of Arizona, 933 N. Cherry Ave., Tucson, AZ 85721, USA; trawle@as.arizona.edu
[2] Institute for Computational Cosmology, Durham University, South Road, Durham DH1 3LE, UK
[3] School of Physics and Astronomy, University of Birmingham, Edgbaston, Birmingham B15 2TT, UK
[4] Herschel Science Centre, ESAC, ESA, P.O. Box 78, Villanueva de la Cañada, 28691 Madrid, Spain
[5] Departamento de Astrofísica, Facultad de CC. Físicas, Universidad Complutense de Madrid, E-28040 Madrid, Spain
[6] Sterrewacht Leiden, Leiden University, P.O. Box 9513, 2300 RA, Leiden, The Netherlands
[7] Department of Physics, Mathematics and Astronomy, California Institute of Technology, Pasadena, CA 91125, USA
[8] Jet Propulsion Laboratory (JPL), National Aeronautics and Space Administration (NASA), Pasadena, CA 91109, USA

ABSTRACT

We present far-infrared (FIR) analysis of 68 brightest cluster galaxies (BCGs) at $0.08 < z < 1.0$. Deriving total infrared luminosities directly from *Spitzer* and *Herschel* photometry spanning the peak of the dust component (24–500 μm), we calculate the obscured star formation rate (SFR). $22^{+6.2}_{-5.3}$% of the BCGs are detected in the far-infrared, with SFR = 1–150 $M_\odot$ yr^{-1}. The infrared luminosity is highly correlated with cluster X-ray gas cooling times for cool-core clusters (gas cooling time <1 Gyr), strongly suggesting that the star formation in these BCGs is influenced by the cluster-scale cooling process. The occurrence of the molecular gas tracing Hα emission is also correlated with obscured star formation. For all but the most luminous BCGs ($L_{TIR} > 2 \times 10^{11} L_\odot$), only a small ($\lesssim$0.4 mag) reddening correction is required for SFR(Hα) to agree with SFR$_{FIR}$. The relatively low Hα extinction (dust obscuration), compared to values reported for the general star-forming population, lends further weight to an alternate (external) origin for the cold gas. Finally, we use a stacking analysis of non-cool-core clusters to show that the majority of the fuel for star formation in the FIR-bright BCGs is unlikely to originate from normal stellar mass loss.

Key words: galaxies: clusters: general – galaxies: elliptical and lenticular, cD – galaxies: star formation – infrared: galaxies

Online-only material: color figures

1. INTRODUCTION

In the central regions of rich galaxy clusters, the intracluster medium (ICM) can be sufficiently dense that cooling to 10^4 K occurs on timescales shorter than the cluster lifetime (Cowie & Binney 1977; Fabian & Nulsen 1977; Edge et al. 1992). However, X-ray observations indicate that at low gas temperatures (a factor of a few below ambient), the cooling rates are slower than expected for a simple run-away cooling flow model (e.g., Tamura et al. 2001; Peterson & Fabian 2006). Active galactic nucleus (AGN) outbursts could inject sufficient energy into the ICM to suppress cooling. Although the underlying physics is still not well understood, observation of radio bubbles, so-called as they are regions relatively empty of thermal X-ray gas coincident with the radio lobes (e.g., Böhringer et al. 1993; McNamara et al. 2000), supports AGN heating as a viable mechanism (Edge et al. 1992; McNamara & Nulsen 2007).

Many clusters possess a large elliptical galaxy at the minimum of the potential well. These brightest cluster galaxies (BCGs) are often more than a magnitude brighter in optical bands than the second ranked galaxy. In contrast to the majority of massive cluster ellipticals, which are optically red and quiescent, some BCGs contain significant cool gas and exhibit signs of star

formation. These BCGs exhibit far-infrared atomic cooling lines (Mittal et al. 2011) and millimeter molecular transitions (H$_2$ and CO emission) that reveal large quantities of gas at a range of cool temperatures ($T \lesssim 2000$ K; Edge et al. 2002; Egami et al. 2006b; Johnstone et al. 2007; Edge et al. 2010b). Strong optical emission lines are often used as a proxy for this molecular gas (e.g., Cavagnolo et al. 2008), with measured line ratios typical of H II regions (Crawford et al. 1999; Conselice et al. 2001). Hα imaging of nearby BCGs appears to show emission tracing filamentary structure well beyond the central AGN, but apparently created by the radio bubbles (e.g., Crawford et al. 2005).

The infrared dust component offers an independent probe of the star formation rate (SFR). In the *Spitzer* era, great sensitivity at 24 μm offered the ability to estimate SFR for large samples of BCGs (e.g., Egami et al. 2006a; Quillen et al. 2008). For instance, using the latter of these samples, O'Dea et al. (2008) found that the cluster X-ray emission is correlated with IR luminosity for Hα-detected BCGs, suggesting that cool gas originally associated with the ICM is fueling star formation in BCGs. This interplay is still not well understood, with only a small fraction of the available cold gas forming stars ($\lesssim 100$ $M_\odot$ yr^{-1}).

With the advent of sensitive far-infrared (FIR) observations from the *Herschel Space Observatory*, it is now, for the first time, possible for a direct measurement of the dust component in a large sample of BCGs. This study uses *Herschel* photometry to calculate the total IR luminosity for BCGs in clusters at

$z \sim 0.08$–1.0. Dust properties and SFR can be constrained tightly, without the need to estimate from the mid-infrared. This is particularly important at these redshifts, as the varying intensity of polycyclic aromatic hydrocarbon (PAH) and silicate absorption features within the $24\,\mu$m band causes nonsystemmatic uncertainty in the extrapolated IR luminosity.

The paper is organized as follows. Section 2 details the far-infrared observations, while Section 3 describes the important process of matching flux at different wavelengths (counterparting) and tabulates the final photometry. Section 4 describes the spectral energy distribution (SED) template fitting procedure and presents the integrated IR luminosities. In Section 5, we discuss the dust and star formation properties in the context of cool-core cluster indicators. The primary conclusions are summarized in Section 6.

2. OBSERVATIONS

This study employs far-infrared data from the ESA *Herschel Space Observatory* (Pilbratt et al. 2010). Specifically, we use photometry from the Photodetector Array Camera and Spectrometer (PACS; Poglitsch et al. 2010) at 70, 100, 160 μm, and from the Spectral and Photometric Imaging Receiver (SPIRE; Griffin et al. 2010) at 250, 350, 500 μm. These bands straddle the peak of the far-infrared SED, for sources up to $z \sim 3$. The respective beam sizes are larger with increasing wavelength, with FWHM = $5\rlap{.}''2$, $7\rlap{.}''7$, $12''$, $18''$, $25''$, and $36''$.

Three *Herschel* key programs contribute to the full sample of 67 cluster fields (68 BCGs): Herschel Lensing Survey (HLS; Egami et al. 2010), Local Cluster Substructure Survey (LoCuSS; Smith et al. 2010), and a study of BCGs in known cool-core clusters (Edge et al. 2010b, E10). *Herschel* data were processed using an augmented version of the standard reduction pipelines (HIPE; Ott 2010). Major modifications are as follows. During PACS reduction, high-pass filtering of the time-stream is necessary to remove the $1/f$ noise drift. In an attempt to avoid bright source ringing, we implement a simple masking algorithm prior to filtering. In all *Herschel* processing, signal-to-noise was maximized by including data frames beyond the nominal science scan legs, based on instantaneous scan speed: within 10% of science scan speed for PACS; $\gtrsim 0\rlap{.}''5\,\mathrm{s}^{-1}$ for SPIRE. In reality, turnaround frames only increase sensitivity at the BCG position for HLS PACS, where the total map size is comparable to a single array footprint. For further details on the *Herschel* data reduction, please refer to the individual survey papers.

The infrared SEDs for each BCG also include, where available, data from the *Spitzer* archive (IRAC and MIPS), the Two Micron All Sky Survey (2MASS) 2.2 μm K-band catalog (Skrutskie et al. 2006), and the *Wide-field Infrared Survey Explorer* (*WISE*; Wright et al. 2010) preliminary data release (at 3.4, 4.6, 12, and 22 μm). Although coverage in these near/mid-infrared bands is not complete, none of our conclusions are sensitive to their availability.

2.1. Herschel Lensing Survey (HLS)

HLS (Egami et al. 2010) was primarily devised to exploit the lensing effect of massive clusters, probing beyond the confusion limit of the *Herschel* instruments to observe intrinsically faint, high-redshift sources (e.g., Rex et al. 2010). HLS comprises deep *Herschel* data in five bands, 100–500 μm. PACS imaging at 100 and 160 μm has mean 3σ limits of 2.4 and 4.7 mJy, while in the three SPIRE bands, the typical 3σ limits are 9.4, 10.6, 12.0 mJy, respectively.

The survey observed 44 clusters ($0.2 < z < 1.0$, with the majority at $0.2 < z < 0.4$) centered on the diffuse X-ray peak. More than three quarters of the clusters are covered by *Spitzer* MIPS 24 μm imaging, nearly all have IRAC data at 3.6 and 4.5 μm, while approximately a third also have 5.8 and 8 μm. Crucially for BCG identification, all of the cluster cores have been observed in at least one *Hubble Space Telescope* (*HST*) band.

2.2. Local Cluster Substructure Survey (LoCuSS)

LoCuSS is a multi-wavelength (X-ray, through far-UV, optical, far-IR, to radio), wide-field survey of X-ray luminous galaxy clusters at $0.15 < z < 0.3$. One of the main motivations is to probe the physics responsible for the transformation of galaxies from late to early types in the cluster infall regions and surrounding large-scale structure (Smith et al. 2010). A key data set supporting this science goal is *Herschel* observations at 100–500 μm of a representative sample of 31 clusters. The data cover a wider field of view ($\sim 25' \times 25'$) than HLS to mean 3σ depths of 13.0, 17.0, 14.0, 18.9, 20.4 mJy (100–500 μm).

The 31 cluster *Herschel* sample is referred to in this paper as LoCuSS. Eleven of the clusters are also in HLS, and for these, we adopt the deeper HLS *Herschel* data. The LoCuSS sample has full coverage in the optical from both *HST* and Subaru Suprime-Cam (Okabe et al. 2010). *Spitzer* MIPS 24 μm photometry is complete (Haines et al. 2009; C. P. Haines et al. 2012, in preparation), while IRAC imaging is available for more than half of the clusters. MIPS 70 μm photometry was published for three LoCuSS BCGs in Quillen et al. (2008).

2.3. Known Cool-core Clusters (E10)

The third component explores far-infrared line emission and continuum properties for a sample of 11 well-studied BCGs in cool-core clusters. The BCGs were selected by optical emission and X-ray properties as the most likely FIR-luminous BCGs in the local universe ($z \lesssim 0.3$). The *Herschel* observations pertinent for this study were published in Edge et al. (2010b, E10) and includes all six PACS+SPIRE bands (70–500 μm) for three BCGs (A1068, Z3146, A2597). These sources have extensive existing optical and infrared photometry, as well as submillimeter observations from the James Clerk Maxwell telescope (JCMT)/SCUBA.

3. MULTI-BAND PHOTOMETRY

In this section, we describe the process of allocating multi-band infrared flux to each optical BCG. This applies to the 64 clusters in the HLS and LoCuSS samples. Photometry for the remaining three BCGs was taken directly from E10.

3.1. BCG identification

For each cluster, the first task was to identify the BCG, which we define as the optically brightest source in the cluster. We verified literature positions by examining all available optical data, including central *HST* imaging in every case. Two of the clusters are generally considered to consist of two components, each with their own BCG: A773 (Crawford et al. 1999) and A1758 (David & Kempner 2004). We confirm this selection, and retain both sources for analysis (labeled north and south). Our conclusions are independent of the inclusion of any combination of these BCGs. MACS0025.4–1222 (the "Baby Bullet") lacks

Table 1
Observed *Herschel* Far-infrared (100–500 μm) Photometry for the 65 BCGs in the HLS and LoCuSS Samples

Cluster ID[a]	α_{BCG}[b]	δ_{BCG}[b]	$z_{cluster}$	H/L[c]	f_{100} (mJy)	f_{160} (mJy)	f_{250} (mJy)	f_{350} (mJy)	f_{500} (mJy)
A2744	00 14 20.7	−30 24 00	0.308	H	<2.4	<4.5	<7.8	<9.2	<10.7
MACS0018	00 18 33.6	+16 26 15	0.541	H	<2.3	<4.8	<10.0	<10.4	<11.4
A0068	00 37 06.9	+09 09 24	0.255	HL	<2.5	<5.0	<12.9	<13.0	<13.3
A2813	00 43 24.7	−20 37 41	0.292	H	<2.4	<4.7	<8.3	<10.0	<11.9
A0115	00 55 50.6	+26 24 37	0.197	L	<13.0	<17.0	<14.0	<18.9	<20.4
Z0348	01 06 49.4	+01 03 22	0.254	L	81.1 ± 2.8	54.7 ± 5.8	35.0 ± 5.2	12.0 ± 4.3	<20.4
A2895	01 18 11.1	−26 58 12	0.227	H	<2.4	<4.7	<7.7	<9.1	<11.1
A0209	01 31 52.5	−13 36 41	0.206	HL	<2.4	<4.7	<7.8	<9.5	<11.0
R0142	01 42 03.4	+21 31 15	0.280	L	<13.0	<17.0	<14.0	<18.9	<20.4
A0267	01 52 41.9	+01 00 27	0.231	HL	<2.5	<4.8	<8.0	<9.6	<11.2
A0291	02 01 43.1	−02 11 47	0.196	L	<13.0	<17.0	<14.0	<18.9	<20.4
RCS0224	02 24 34.2	−00 02 32	0.773	H	<2.3	<4.7	<8.4	<9.6	<10.9
A0368	02 37 27.8	−26 30 29	0.220	H	<2.5	<4.6	<7.7	<8.9	<10.2
A0383	02 48 03.4	−03 31 44	0.187	HL	12.3 ± 0.1	32.5 ± 0.5	14.9 ± 6.3	14.6 ± 6.0	<10.6
A3084	03 04 03.9	−36 56 27	0.219	H	<2.4	<4.4	<7.7	<9.1	<10.7
A3088	03 07 02.1	−28 39 58	0.253	H	6.9 ± 0.2	6.1 ± 0.5	<7.0	<8.5	<10.1
MACS0451	04 51 54.6	+00 06 18	0.430	H	<2.3	<4.2	<13.0	<15.6	<19.5
A0521	04 54 06.9	−10 13 24	0.253	H	<2.3	<4.5	<9.4	<10.2	<11.9
AS0592	06 38 45.2	−53 58 22	0.222	H	<2.4	<4.7	<15.3	<15.7	<16.3
MACS0647	06 47 50.7	+70 14 54	0.591	H	<2.3	<4.8	<14.7	<14.2	<14.5
BULLET	06 58 38.1	−55 57 26	0.296	H	<3.1	<5.8	<8.2	<9.6	<12.4
MACS0717	07 17 37.2	+37 44 23	0.546	H	<2.3	<4.3	<10.5	<11.1	<11.7
A0586	07 32 20.3	+31 38 01	0.171	L	<13.0	<17.0	<14.0	<18.9	<20.4
Z1432	07 43 23.1	+17 33 42	0.111	L	<13.0	<17.0	⋯	⋯	⋯
MACS0744	07 44 52.8	+39 27 25	0.698	H	<2.3	<4.6	<7.9	<9.5	<10.7
A0611	08 00 56.8	+36 03 24	0.288	H	<2.3	<4.5	<8.8	<9.6	<10.7
Z1693	08 25 57.8	+04 14 48	0.225	L	<13.0	<17.0	<14.0	<18.9	<20.4
A0665	08 30 57.3	+65 50 32	0.182	L	<13.0	<17.0	<14.0	<18.9	<20.4
A0689	08 37 24.6	+14 58 22	0.279	L	⋯	⋯	<14.0	<18.9	<20.4
Z1883	08 42 55.9	+29 27 27	0.194	L	15.3 ± 2.2	15.4 ± 2.9	10.2 ± 5.2	<18.9	<20.4
A0697	08 42 57.6	+36 22 00	0.282	HL	<2.3	<4.2	<8.2	<10.0	<11.7
Z2089	09 00 36.9	+20 53 40	0.235	L	55.5 ± 2.5	24.3 ± 2.9	12.4 ± 5.2	5.8 ± 4.3	<20.4
A0773S	09 17 53.4	+51 43 39	0.217	H	<2.4	<4.3	<8.0	<9.6	<11.2
A0773N	09 17 53.5	+51 44 01	0.217	H	<2.4	<4.3	<8.0	<9.6	<11.2
A0851	09 42 57.5	+46 58 50	0.407	H	23.7 ± 0.3	25.3 ± 0.7	20.5 ± 5.5	12.3 ± 6.2	<11.0
A0868	09 45 26.4	−08 39 07	0.153	H	<2.4	<5.2	<7.7	<8.9	<10.6
Z2701	09 52 49.2	+51 53 06	0.214	H	<2.4	<4.7	<7.1	<8.2	<9.8
A0963	10 17 03.6	+39 02 49	0.206	HL	<2.5	<4.9	<7.9	<10.0	<11.2
MACS1149	11 49 35.7	+22 23 55	0.544	H	<2.4	<4.4	<7.6	<9.0	<10.5
A1413	11 55 17.8	+23 24 16	0.143	H	<2.4	<4.6	<7.7	<8.9	<10.6
A1689	13 11 29.5	−01 20 28	0.183	L	<13.0	<17.0	<14.0	<18.9	<20.4
A1703	13 15 05.3	+51 49 02	0.281	H	<2.4	<4.5	<7.9	<9.4	<11.8
A1758N	13 32 38.4	+50 33 35	0.279	HL	<2.4	<4.9	<8.0	<9.4	<11.3
A1758S	13 32 52.1	+50 31 34	0.279	HL	<2.4	<4.9	<8.0	<9.4	<11.3
A1763	13 35 20.1	+41 00 04	0.228	L	<13.0	<17.0	<14.0	<18.9	<20.4
A1835	14 01 02.1	+02 52 43	0.253	L	315.1 ± 1.8	322.6 ± 2.9	122.0 ± 5.2	45.9 ± 4.3	21.5 ± 6.2
MACS1423	14 23 47.9	+24 04 42	0.543	H	13.0 ± 0.1	27.7 ± 0.3	20.8 ± 4.6	14.4 ± 5.8	<10.2
A1914	14 25 56.6	+37 48 59	0.171	HL	<2.5	<5.0	<7.9	<9.0	<11.0
Z7160	14 57 15.1	+22 20 35	0.258	L	<13.0	<17.0	<14.0	<18.9	<20.4
A2218	16 35 49.1	+66 12 44	0.171	L	<13.0	<17.0	<14.0	<18.9	<20.4
A2219	16 40 19.8	+46 42 42	0.228	L	<13.0	<17.0	<14.0	<18.9	<20.4
RXJ1720	17 20 10.1	+26 37 32	0.164	HL	9.3 ± 0.1	7.2 ± 0.9	<13.6	<14.5	<16.2
A2345	21 27 13.7	−12 09 46	0.176	L	<13.0	<17.0	<14.0	<18.9	<20.4
MACS2129	21 29 26.2	−07 41 29	0.589	H	<2.4	<5.3	<29.7	<27.7	<27.2
RXJ2129	21 29 40.0	+00 05 21	0.235	HL	3.9 ± 0.1	6.5 ± 0.3	7.1 ± 1.8	<10.1	<12.0
MS2137	21 40 15.1	−23 39 40	0.313	H	<2.4	<4.6	<8.0	<9.3	<10.3
A2390	21 53 36.8	+17 41 45	0.233	L	17.5 ± 2.4	38.6 ± 5.7	31.4 ± 5.2	20.4 ± 4.3	8.2 ± 6.2
A2485	22 48 31.1	−16 06 26	0.247	L	<13.0	<17.0	<14.0	<18.9	<20.4
AS1063	22 48 44.0	−44 31 51	0.348	H	<2.3	<4.3	<8.0	<9.9	<11.5
AS1077	22 58 48.3	−34 48 07	0.312	H	<2.4	<4.6	<8.0	<9.2	<10.0
A2537	23 08 22.3	−02 11 33	0.295	H	<2.5	<5.1	<11.9	<12.8	<12.6
RCS2319	23 19 53.4	+00 38 13	0.897	H	<2.3	<4.5	<7.7	<9.0	<10.4
RCS2327	23 27 27.6	−02 04 37	0.700	H	<2.5	<4.8	<9.6	<11.0	<13.5

Table 1
(Continued)

Cluster ID[a]	α_{BCG}[b]	δ_{BCG}[b]	$z_{cluster}$	H/L[c]	f_{100} (mJy)	f_{160} (mJy)	f_{250} (mJy)	f_{350} (mJy)	f_{500} (mJy)
A2631	23 37 39.7	+00 16 17	0.273	H	<2.4	<4.7	<8.2	<9.5	<10.8
A2667	23 51 39.4	−26 05 03	0.230	H	20.4 ± 0.1	27.4 ± 0.4	10.6 ± 2.6	<9.5	<11.9

Notes. Non-detections denoted by the 3σ limit.
[a] Cluster name, including A/B designation (as in the literature) for multiple candidate BCGs in a single cluster.
[b] Position of the BCG in optical (*HST*) imaging.
[c] Subsample: H, HLS; L, LoCuSS. For clusters in both samples, HL is shown for reference, although the deeper HLS *Herschel* images have provided the photometry.

an obvious BCG and is removed from the sample. The left-most columns in Table 1 present the clusters and supply optical positions for the 65 BCGs (including two pairs).

3.2. Counterparts

The PACS beam size (∼8 arcsec) has a large probability of encompassing multiple optical sources. The most effective method of evaluating whether long-wavelength flux is associated with an optical source is to "step through" the wavelength range using all available near- and mid-infrared data. It is important to note that a priori knowledge or expectation of whether a particular BCG should emit in the far-infrared was not used during the allocation of flux to sources.

In all cases, the BCG is identifiable in the 2MASS and *Spitzer* IRAC near-infrared bands, when such data are available (only seven BCGs lack IRAC coverage), providing a useful link between optical and far-infrared wavelengths. In many cases, there are no *Spitzer* 24 μm or *Herschel* sources near the optical BCG position, and the BCG clearly decreases in luminosity through the IRAC bands (e.g., Figures 1(a) and (b)). In a few instances, a single mid-infrared source is located in the immediate vicinity of the optical BCG position, but on closer examination, this flux obviously originates from a secondary IRAC source (e.g., Figure 1(c)).

A few clusters contain single, point-source FIR counterparts to the BCG (e.g., Figure 1(d)). However, many of the *Herschel*-detected BCGs require the subtraction of secondary sources in at least the longer SPIRE bands where the spatial resolution deteriorates (e.g., Figures 1(e) and (f)). The techniques employed for extracting flux, particularly in such blended and confused cases, are described in the next section.

3.3. Photometry

Photometry for *Spitzer* and PACS, where blending and source confusion is minimal, was obtained using simple aperture photometry via the SExtractor package (Bertin & Arnouts 1996). Aperture corrections were applied individually in each band, based on instrument handbook values or the latest model beam profiles.

In the SPIRE bands, background source confusion is above the instrumental noise. Photometry for all sources within ∼3 arcmin of the BCG was extracted using the IRAF routine ALLSTAR. This algorithm fits the known point-spread function (PSF) to all positions in an input source catalog, thereby measuring photometry for all potential sources simultaneously. Any significant contaminating flux within a beam of the BCG position should be accounted for. Where available, MIPS 24 μm is the favored input catalog, as the majority of *Herschel* point sources have visible counterparts in the MIPS image. Otherwise,

the longest available wavelength IRAC band is used instead (although the correspondence between IRAC and FIR is not as consistent). While residual flux from confused background sources, too faint for inclusion in the MIPS catalog, may boost the SPIRE flux, use of such an a priori catalog should minimize the effect. Statistical de-boosting is beyond the scope of this study.

Table 1 presents the *Herschel* fluxes (100–500 μm) for the HLS and LoCuSS sample BCGs. Non-detections are indicated by the 3σ detection limit of each map (note the significant difference in depth between HLS and LoCuSS data). Overall, 37 of the 65 BCGs in HLS+LoCuSS are detected at 24 μm. A further seven BCGs lack observations at this wavelength. However, in all such cases the slope of the IRAC photometry together with non-detections in PACS suggests no significant infrared component (SFR $< 2 M_\odot$ yr^{-1}). Of the 37 MIPS sources, 12 are detected in both PACS bands (there are no sources in a single *Herschel* band only). Ten of these BCGs are also detected by SPIRE at 250 μm, seven at 350 μm, while two have significant flux at 500 μm.

4. SED ANALYSIS AND RESULTS

In this section, we analyze the full sample of 68 BCGs (65 HLS+LoCuSS; 3 from E10), ensuring a homogeneous characterization of the far-infrared component.

4.1. Infrared SED fitting

Far-infrared dust properties are derived from the best-fitting template across all photometric data $\lambda_{obs} \geqslant 24$ μm. We employ weighted fits to the recent templates from Rieke et al. (2009, R09). These templates are derived from 11 star-formation-dominated local (ultra-)luminous IR galaxies (LIRGs) with high quality data across the infrared wavelengths, which were combined and interpolated to produce a library of spectra for galaxies at specific luminosity. Recently, inconsistencies have been discovered between the shape of the FIR component in these local sources and more distant galaxy populations. For instance, luminous sources at high redshift appear to be fit better by local templates of lower luminosity (e.g., Rex et al. 2010), while a subset of cluster member galaxies have warmer dust than expected for their luminosity and are better fit by higher luminosity templates (Rawle et al. 2010; T. D. Rawle et al. 2012, in preparation). Here, we are primarily interested in the total infrared luminosity, and so disregard the nominal luminosity class of the templates, simply integrating the template which best fits the observed shape of the dust component (with appropriate normalization).

Total infrared luminosity (L_{TIR}) is calculated by integrating the best-fit template over the (rest frame) wavelength range
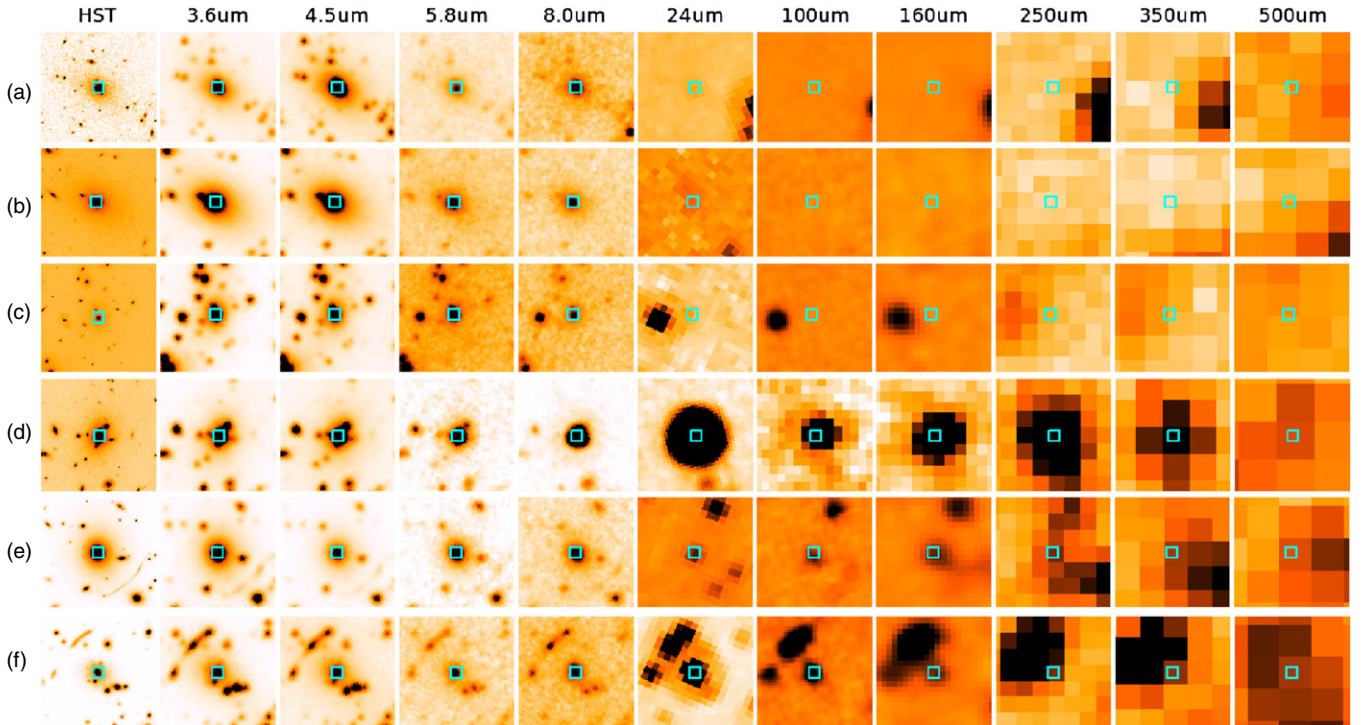
Figure 1. Eleven-band thumbnails (*HST*, IRAC, MIPS, PACS, SPIRE) for a representative selection of BCGs, identified by the cyan square (each frame is $40'' \times 40''$): (a) AS1063, (b) A1914, (c) A2744, (d) A1835, (e) A383, and (f) A2667. See Section 3.2 for details.

(A color version of this figure is available in the online journal.)

$\lambda_0 = 8$–$1000\,\mu$m. Uncertainty in luminosity is estimated by repeating the full fitting procedure for many Monte Carlo realizations of the observed photometric data. SFR is derived directly from $L_{\rm TIR}$ following the simple relation of Kennicutt (1998).[10] Figures 9–11 in the Appendix present the observed FIR SED for *Herschel*-detected BCGs and indicate the best-fit templates and subsequent values for $L_{\rm TIR}$ and SFR.

As a sanity check, $L_{\rm TIR}$ and SFR are also derived using the templates from Chary & Elbaz (2001) and Dale & Helou (2002). The best-fitting template from both are selected as described above for R09. SFRs derived from these template sets agree with the R09 values within 6% and 2%, respectively (Figure 2). All three template libraries are unable to match the observed FIR and $24\,\mu$m simultaneously for a significant number of sources. This is most likely due to PAH and/or silicate absorption features within the MIPS $24\,\mu$m band (rest frame $\lambda_0 \approx 16$–$20\,\mu$m at these redshifts). SFR can be estimated directly from the $24\,\mu$m flux, following Equation (14) from Rieke et al. (2009). SFR$_{24}$ disagrees with the *Herschel*-derived SFR (from integrated $L_{\rm TIR}$) by an average of 20% (Figure 2). The major outlier (Z2089; SFR $\sim 0.05 \times$ SFR$_{24}$) is described further in subsequent sections.

Characteristic dust temperature is calculated via a modified blackbody of the form

$$S_\nu = N\nu^\beta B_\nu(T_{\rm dust}), \qquad (1)$$

where S_ν is flux density, β is dust emissivity index (fixed at 1.5), and $B_\nu(T_{\rm dust})$ is the Planck blackbody radiation function for a source at characteristic temperature $T_{\rm dust}$. $\beta T_{\rm dust}$ remains approximately constant (Blain et al. 2003), so fixing $\beta = 2.0$ instead would systematically lower the derived temperature (by

---

[10] SFR$_{\rm IR}$ ($M_\odot$ yr^{-1}) $= 4.5 \times 10^{-44}\, L_{\rm IR}$ (erg s^{-1}).
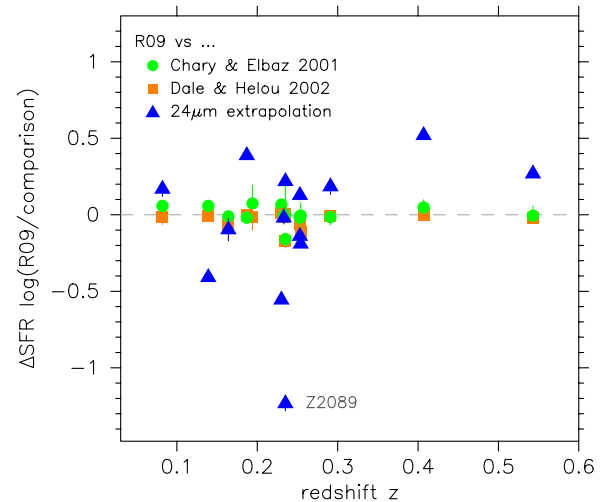

Figure 2. For FIR-bright BCGs, obscured SFR derived using the Rieke et al. (2009, R09) templates compared to SFRs derived from Chary & Elbaz (2001, green circles) and Dale & Helou (2002, orange squares) templates, and from extrapolating the $24\,\mu$m flux via Equation (14) of Rieke et al. (blue triangles). All ΔSFRs are plotted as a function of BCG redshift, with the majority of errors well within the symbol size. The labeled major outlier (SFR$_{24} \gg$ SFR$_{\rm R09}$) is Z2089.

(A color version of this figure is available in the online journal.)

$\sim$3 K at 30 K). Photometry at wavelengths shorter than $100\,\mu$m is not used in the blackbody fit.

Fits for two modified blackbodies, as employed in E10, are strongly dependent on the inclusion of $24\,\mu$m. With the mid-infrared, best-fit temperatures tend toward $\sim$20 K and $\sim$50 K, with much the same $L_{\rm TIR}$ as the best-fitting template. Excluding $24\,\mu$m, the fits are less constrained and the two components become more similar ($\sim$30–40 K), or one component becomes insignificant and the solution tends toward the single

Table 2
Derived SED Parameters for *Herschel* and/or Hα-detected BCGs

Cluster ID[a]	H/L/E[b]	$L_{\rm TIR}(24)$[c] ($L_\odot$)	SFR_{24}[c] ($M_\odot$ yr^{-1})	$L_{\rm TIR}$(FIR)[d] ($L_\odot$)	$SFR_{\rm FIR}$[d] ($M_\odot$ yr^{-1})	$L({\rm H\alpha})$[e] log(erg s^{-1})
Z0348	L	$2.9 \pm 0.07 \times 10^{11}$	50.5 ± 1.1	$1.9 \pm 0.06 \times 10^{11}$	32.6 ± 1.2	42.50
A0383	HL	$9.4 \pm 0.51 \times 10^{9}$	1.6 ± 0.1	$2.3 \pm 0.10 \times 10^{10}$	4.0 ± 0.2	41.85
A3088	H	$1.3 \pm 0.03 \times 10^{10}$	2.2 ± 0.1	$1.8 \pm 0.06 \times 10^{10}$	3.0 ± 0.1	41.30
Z1883	L	$<1.3 \times 10^{10}$	<2	$2.4 \pm 0.32 \times 10^{10}$	4.1 ± 0.5	42.14
Z2089	L	$2.0 \pm 0.12 \times 10^{12}$	346.4 ± 20.6	$1.2 \pm 0.06 \times 10^{11}$	20.2 ± 1.0	42.50
A0851	H	$5.7 \pm 0.19 \times 10^{10}$	9.9 ± 0.3	$1.9 \pm 0.09 \times 10^{11}$	32.7 ± 1.6	$\cdots$
Z3146	E	$3.5 \pm 0.34 \times 10^{11}$	61.0 ± 6.0	$5.4 \pm 0.29 \times 10^{11}$	93.1 ± 5.1	42.55
A1068	E	$1.5 \pm 0.04 \times 10^{12}$	254.4 ± 6.8	$5.8 \pm 0.03 \times 10^{11}$	99.3 ± 0.5	41.94
A1835	L	$1.2 \pm 0.01 \times 10^{12}$	202.0 ± 0.5	$8.5 \pm 0.05 \times 10^{11}$	146.5 ± 0.8	42.20
MACS1423	H	$1.4 \pm 0.04 \times 10^{11}$	24.8 ± 0.7	$2.7 \pm 0.17 \times 10^{11}$	46.0 ± 2.9	42.00
RXJ1720	HL	$1.2 \pm 0.19 \times 10^{10}$	2.0 ± 0.3	$9.3 \pm 0.27 \times 10^{9}$	1.6 ± 0.1	40.88
RXJ2129	HL	$6.0 \pm 0.25 \times 10^{9}$	1.0 ± 0.1	$1.0 \pm 0.05 \times 10^{10}$	1.7 ± 0.1	40.75
A2390	L	$5.1 \pm 0.03 \times 10^{10}$	8.8 ± 0.1	$4.9 \pm 0.49 \times 10^{10}$	8.5 ± 0.7	41.69
A2597	E	$1.2 \pm 0.12 \times 10^{10}$	2.1 ± 0.2	$1.8 \pm 0.05 \times 10^{10}$	3.1 ± 0.1	41.48
A2667	H	$1.8 \pm 0.02 \times 10^{11}$	31.2 ± 0.3	$5.0 \pm 0.14 \times 10^{10}$	8.7 ± 0.2	41.60
A0115	L	$1.8 \pm 0.04 \times 10^{10}$	3.0 ± 0.1	$<2.5 \times 10^{10}$	<4	41.03
A0291	L	$1.8 \pm 0.04 \times 10^{10}$	3.2 ± 0.1	$<2.5 \times 10^{10}$	<4	41.36
Z2701	H	$<4.2 \times 10^{9}$	<1	$<6.4 \times 10^{9}$	<1	40.64
Z7160	L	$2.4 \pm 0.04 \times 10^{10}$	4.2 ± 0.1	$<4.2 \times 10^{10}$	<9.6	41.40

Notes. BCGs listed beneath the dividing line were not detected in any of the FIR *Herschel* bands, but do have a measured Hα emission line flux.
[a] Cluster ID as in Table 1.
[b] Subsample: H, HLS; L, LoCuSS; E, Edge et al. (2010b). Clusters in both HLS and LoCuSS are indicated, although the deeper HLS *Herschel* provided the photometry.
[c] Estimated from the 24 μm photometry (via Rieke et al. 2009).
[d] Derived from the best-fit Rieke et al. (2009) template.
[e] Literature Hα luminosity.

modified blackbody. At most, only six of our BCG samples (including all three from E10) have sufficient photometry to fit a well-constrained two-component model. We avoid two component blackbodies in favor of the single characteristic temperature and $L_{\rm TIR}$ derived from the best-fitting template.

Template and blackbody fitting is only employed for BCGs with a detection in at least two *Herschel* bands (although in practice, no sources have a detection in only one band). For the remaining BCGs, an upper limit on $L_{\rm TIR}$, and hence SFR, can be calculated from the *Herschel* detection limits. The detection limits are significantly different for each survey (but relatively stable map-to-map within a sub-sample, e.g., 1σ deviation in the HLS limits is 0.1 and 0.3 mJy for the two PACS bands), and the limit for $L_{\rm TIR}$ is also a function of redshift. An additional limit on luminosity is estimated from the 24 μm data (where available) and is used in subsequent figures if it presents a tighter constraint than the *Herschel*-derived limit.

4.2. Total infrared luminosities

The upper portion of Table 2 presents $L_{\rm TIR}$ and SFR (as derived from the R09 fits) for all *Herschel*-detected BCGs in the sample. The 24 μm derived values are shown for completeness. The majority of BCGs in this sample are not luminous in the far-infrared (Figure 3). Only 15 of the 68 BCGs ($22^{+6.2}_{-5.3}$%) are confirmed as $L_{\rm TIR} \gtrsim 10^{10}$ $L_\odot$ (SFR $\gtrsim 2$ $M_\odot$ yr^{-1}), all in the redshift range $0.05 < z < 0.6$. The absolute fraction agrees approximately with previous studies using *Spitzer* mid-infrared data alone: 27^{+20}_{-14}% from Egami et al. (2006a) and 43^{+8}_{-7}% from O'Dea et al. (2008). The difference likely results from the *Herschel* detection limit of our data compared to the 24 μm sensitivity and from the Hα selection used by Quillen et al. (2008) and O'Dea et al., which implicitly

favors cool-core clusters. Seven BCGs ($10^{+5.4}_{-3.4}$%) are LIRGs (i.e., $L_{\rm TIR} > 10^{11}$ $L_\odot$; SFR $\gtrsim 20$ $M_\odot$ yr^{-1}), a similar fraction to the 15% ± 5% from O'Dea et al. The brightest BCG in our sample is A1835 with an $L_{\rm TIR} = 8.5 \times 10^{11}$ $L_\odot$.

The combined cluster sample is in no sense complete, with a bias toward the most massive and well-studied clusters (primary targets for lensing) and containing three BCGs specifically selected due to their anticipated high FIR luminosity. The 31 LoCuSS clusters can be considered statistically identical to a volume-limited sample selected on X-ray luminosity only (see Smith et al. 2010 for more details). The clusters within LoCuSS (including the 11 overlapping with HLS) contain 32 BCGs, eight of which are detected in the far-infrared. This fractional value ($25^{+10.0}_{-8.2}$%) is very similar to our full BCG sample. However, an additional three LoCuSS BCGs have a 24 μm estimated $L_{\rm TIR} > 10^{10}$ $L_\odot$, but fall below the *Herschel* detection limit. Including these, the fraction of star-forming BCGs in the LoCuSS sample (SFR > 2 $M_\odot$ yr^{-1}) is $34^{+10.4}_{-9.7}$%.

The nominal detection limits for each sample are also illustrated in Figure 3, and they effectively vary with redshift as a power law, meaning the observations probe ~2.5 dex in $L_{\rm TIR}$ deeper for the closest clusters ($z \sim 0.1$) than the most distant ($z \sim 1.0$). The *Herschel* observations for HLS probe $L_{\rm TIR} > 10^{10}$ $L_\odot$ for all clusters $z \lesssim 0.35$. The variation of the detection limit, combined with the small number of detections and overabundance of sources at $z \sim 0.2$–0.3 (due to the LoCuSS selection criterion), makes it difficult to comment on possible evolution over time.

4.3. AGN Contamination

Near- and mid-infrared studies have reported that IR-bright BCGs show decreasing flux through the IRAC bands, as
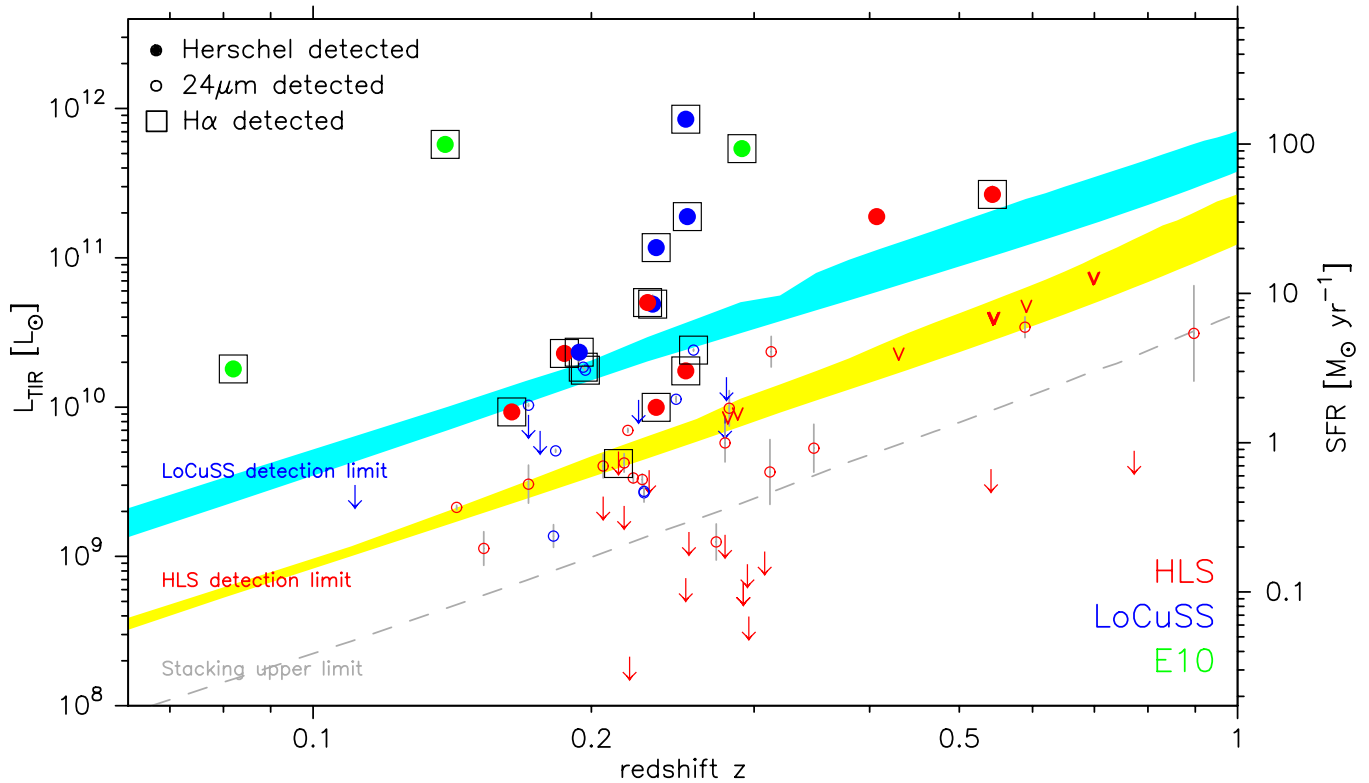
Figure 3. Total infrared luminosity, L_{TIR}, vs. redshift for each BCG: red, HLS; blue, LoCuSS; green, E10. (Red if both HLS and LoCuSS, as HLS data used). Large filled circles denote sources detected by *Herschel*. Smaller open circles show L_{TIR} estimated from 24 μm (for *Herschel* non-detections). "v"-shape and arrow symbols indicate sources undetected by *Herschel*: the former having L_{TIR} upper limits calculated from *Herschel* detection limits, while the latter have tighter constraints derived from 24 μm. Note that all points have associated errors, but the majority lie within the symbol size. BCGs with detected Hα emission are highlighted with an open square, and there is generally a good correspondence between FIR and Hα detections (see Section 5.1). Shaded areas represent the luminosity limit (as a function of redshift) based on the nominal depth of the *Herschel* data: yellow, HLS; cyan, LoCuSS. The width of these areas results from scatter in individual map detection limits and the variation in templates of different luminosity from Rieke et al. (2009). The gray dashed line shows the mean upper limit on L_{TIR} of BCGs without Hα emission, as derived from the stacking analysis (see Section 5.2 for details).

(A color version of this figure is available in the online journal.)

expected for a stellar dominated SED (e.g., Egami et al. 2006a). In contrast, an AGN-dominated source would exhibit a power-law increase through the near-infrared. The majority of BCGs in this present sample also appear to be dominated by the stellar component, and L_{TIR} estimated from 24 μm does not contradict the *Herschel* detection limits. MS2137 ($z = 0.31$) is an exception to this trend, with a luminosity estimate from 24 μm ~ 0.5 dex higher than the nominal detection limit of the *Herschel* data. The IRAC bands suggest that this is not due to a dominant AGN. We return to this sources in Section 5.1.

Z2089 is the one BCG to show a clear power-law increase from ~5–70 μm (in IRAC/MIPS and *WISE* photometry). The IRS spectrum (E. Egami et al. 2012, in preparation) confirms a power-law continuum increase for 5–35 μm, while optical spectroscopy (MMT Hectospec; M. J. Pereira et al. 2012, in preparation) shows broad emission and line ratios suggestive of a strong AGN. The SED for Z2089 shows a large discrepancy between MIPS 70 μm and the *Herschel* observations (almost a magnitude lower in *Herschel*; see Figure 10). IRAC, *WISE*, and 24 μm are tracking the AGN component continuum seen in the IRS spectrum (SFR$_{24}$ = 432 $M_\odot$ yr^{-1} without accounting for an AGN). However, it is likely that 70 μm is substantially boosted by bright [O III], [N III], and/or [O I] emission lines (at λ_{rest} = 51.8, 57.3, 63.3, respectively) which lie within the 70 μm band at $z \sim 0.24$. An alternate explanation is that the notoriously shallow *Spizer* 70 μm imaging (in this case from Quillen et al. 2008) has given an erroneous detection. Even if that were the

case, the FIR peak would have to be particularly broad, or blue, to encompass the *WISE*/24 μm and PACS data. This highly discrepant 70 μm point makes it difficult to include *Spitzer* data in the SED fitting procedures, and the AGN component is much less dominant beyond 100 μm. Therefore, our *Herschel*-derived L_{TIR} (~20 $M_\odot$ yr^{-1}) is a very poor fit $\lambda_{\mathrm{obs}} \leqslant 70$ μm, but is likely to be representative of the true obscured SFR (and is at least a much tighter upper limit).

Optical emission line ratios indicate that A1835 and to a lesser extent A1068 may have sub-dominant contributions from AGNs (Quillen et al. 2008; Donahue et al. 2011). In contrast to Z2089, these AGN components are not identifiable from IRAC colors, the star formation dominated templates fit well at longer wavelengths, and the dust temperatures are reasonable given the FIR luminosity. SFR$_{\mathrm{FIR}}$ is unlikely to be boosted significantly.

4.4. General Dust Properties

We briefly explore the general dust characteristics of the FIR-bright BCG population. The modified blackbody fit to far-infrared data reveals a typical range of dust temperatures 20–40 K (Figure 4). As expected for a source with a strong AGN component, the dust temperature of Z2089 is elevated relative to the normal star-forming population. Excluding Z2089, and accounting for the small sample size, there is no apparent evolution of BCG dust temperature with redshift. There is a wide range in SFRs, with the three most active attaining SFR $\gtrsim$ 100 $M_\odot$ yr^{-1}, although as previously stated, two of these may
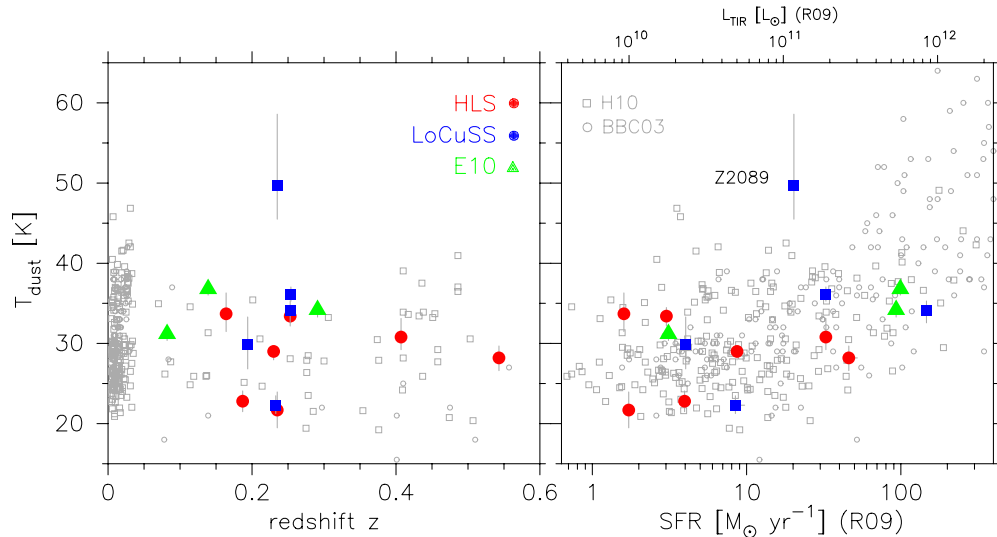
Figure 4. Characteristic dust temperature, as derived from a single modified blackbody fit to the *Herschel* observations, as a function of redshift (left panel) and SFR (right panel) for the FIR-bright BCG sample (large colored points). In the right-hand panel, the equivalent total infrared luminosity is also shown for reference. The normal star-forming galaxy samples from Blain et al. (2003) and Hwang et al. (2010) are plotted as open gray symbols for comparison: in the left panel, restricted to $L_{TIR} < 3 \times 10^{11} L_{\odot}$ as for a typical BCG; in the right panel restricted to $z < 0.6$. The majority of these star-forming sources are in the local universe ($z < 0.05$). The exceptionally warm source is the AGN-dominated BCG Z2089.

(A color version of this figure is available in the online journal.)

include a modest AGN contribution. As expected from simple models of dust heating and confirmed by almost a decade of observations (e.g., Blain et al. 2003; Hwang et al. 2010), the most actively star-forming galaxies typically have warmer dust (gray symbols in Figure 4). In our BCG sample, the LIRG-type BCGs ($L_{TIR} > 10^{11} L_{\odot}$) are on average ∼5 K warmer than the sub-LIRGs. Generally, BCGs (other than the IR-bright AGN host, Z2089) are indistinguishable from normal star-forming galaxies in this parameter space.

5. DISCUSSION

5.1. Comparison to Cool-core Diagnostics

Separation of cool-core and non-cool-core clusters can be difficult and often contentious. The X-ray cooling time is a clean primary indicator of cool gas in the cluster center (Hudson et al. 2010). We follow the relation from Donahue et al. (2005) for pure free–free cooling:

$$t_{c0}(K_0) \sim 10^8 \text{ yrs} \left(\frac{K_0}{10 \text{ keV cm}^2} \right)^{3/2} \left(\frac{kT_X}{5 \text{ keV}} \right)^{-1}, \quad (2)$$

where K_0 is the central entropy derived from a simple power-law profile and kT_X is the mean X-ray gas temperature. The ACCEPT Chandra archival survey (Cavagnolo et al. 2009) presents both K_0 and kT_X for 50 of the 66 clusters in our sample (including 12 of 14 containing FIR-bright BCGs). Figure 5 compares L_{TIR} to this cooling time and shows a very good anti-correlation for the *Herschel*-detected BCGs ($t_{c0} \lesssim 1$ Gyr). This confirms the relation (based on 24 μm extrapolated L_{TIR}) presented in O'Dea et al. (2008, Figure 9) and strongly suggests that the obscured star formation in BCGs is connected to the cluster-scale cooling process.

Ideally we would like to compare the rate of mass deposited ($\dot{M}$) by the cooling central ICM to the condensation rate as traced by SFR. For a small sample of *Spitzer*-detected BCGs, O'Dea et al. (2008) show (in their Figure 10) that $\dot{M}$ is ∼0.5–2

orders of magnitude higher than the SFR. This suggests that the cooling ICM is a plausible origin for the star formation fuel. Computing homogeneous central mass deposition rates for our entire cluster sample (based on, e.g., ACCEPT data) remains a priority but is beyond the scope of this current paper.

Section 4.3 identifies three of the most IR-luminous BCGs as possible hosts of mid-infrared bright AGNs. One may worry that they are so FIR-bright purely because of the contribution of the AGN heating. However, these BCGs are also located in clusters with very short cooling times (<200 Myr), and if the correlation in Figure 5 is real, then they would be expected to be among the most highly star forming. The apparent correlation (albeit very small number statistics) between the BCGs with the highest SFR and those with the strongest radiative AGN may be further evidence (e.g., Egami et al. 2006a) that substantial cooling of intracluster gas in the cluster core modifies the state of the AGN, part of the cyclic interplay between cooling and heating within AGN feedback (e.g., Silk & Rees 1998; Bower et al. 2006).

We now turn to the cold molecular gas itself, directly detectable using millimeter spectroscopy (e.g., Edge 2001; Salomé & Combes 2003). However, even with the advent of *Herschel* spectroscopy in the far-infrared (Edge et al. 2010a), sensitivity severely restricts the sample of potential BCG targets. In this analysis, we opt to use Hα line emission, a known and reliable indicator of ∼10^4 K molecular gas (e.g., Crawford et al. 1999; Cavagnolo et al. 2008). The Hα observations are from a mix of imaging and spectroscopic observations: Donahue et al. (1992), Crawford et al. (1999), Quillen et al. (2008), the Sloan Digital Sky Survey (Adelman-McCarthy et al. 2008), and the REFLEX BCG sample (PI: Edge).

Eighteen of the 68 BCGs ($26^{+6.4}_{-5.7}$%) have detected Hα line emission (highlighted by squares in Figures 3 and 5) agreeing well with the absolute fraction reported by previous large Hα surveys (e.g., 27% ± 4% for 203 BCGs from Crawford et al. 1999). The generally good correspondence between *Herschel* detection and those with measured Hα emission (78% of
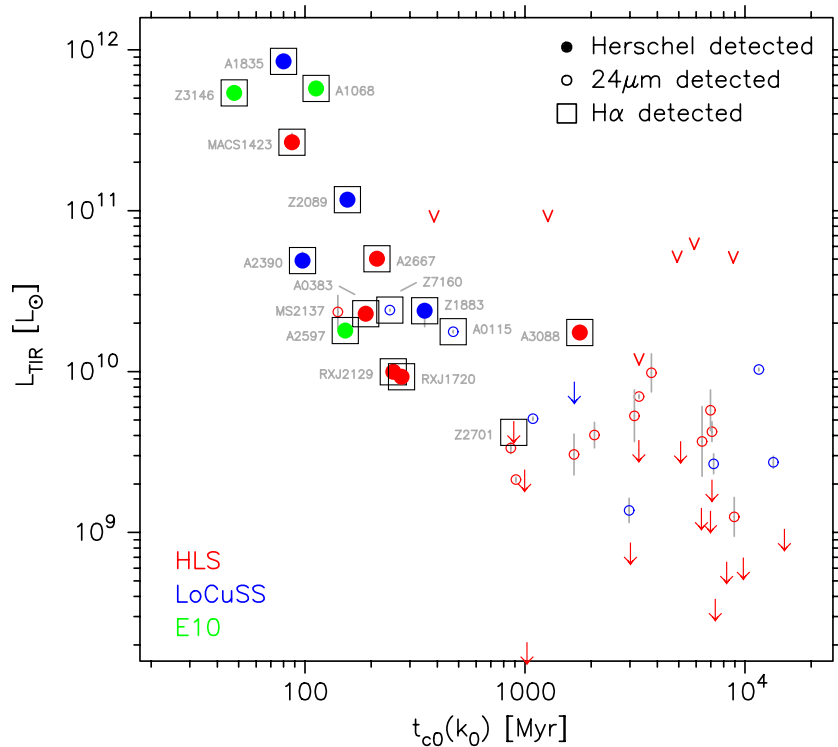
Figure 5. L_{TIR} (from R09 templates) vs. the central X-ray cooling time $t_{c0}(K_0)$ derived from the ACCEPT *Chandra* archive (Cavagnolo et al. 2009) entropy profiles. Solid circles are *Herschel* detections; open circles are 24 μm detected only; "v" and arrows for upper-limits from *Herschel* and 24 μm, respectively. Colors as in Figure 3. BCGs with detected Hα emission are highlighted with an open square and labeled. For $t_{c0}(K_0) < 1$ Gyr, there is a very good correlation between IR luminosity and cooling time.

(A color version of this figure is available in the online journal.)

Hα-detections are FIR sources, while 93% of FIR sources have Hα detections; Figure 3) suggests that the two measurements are probing the same phenomenon and are reaching a comparable depth. Four Hα detections originate from BCGs undetected by *Herschel* (the properties of these are listed below the dividing line in Table 2). Three of these sources are covered by the shallower LoCuSS far-infrared observations, and $L_{TIR}(24 \mu m)$ indicates that they are only marginally below the *Herschel* detection limit. The remaining BCG in this category (Z2701) has a very low $L(H\alpha)$ (>0.6 dex below any other detection). The Hα sources undetected by *Herschel* do not, therefore, contradict an FIR–Hα connection. Only one BCG (A851) is detected by *Herschel* but not in Hα; we return to this source in the final paragraph of the section.

There is a very good correspondence between Hα detection and short cooling times (Figure 5). Almost all BCGs in clusters with $t_{c0}(K_0) < 1$ Gyr are detected in Hα, confirming that the emission is indeed a good indicator of a cool-core cluster (as used in, e.g., Cavagnolo et al. 2008; McDonald et al. 2011). The one notable exception is MS2137, which is not detected by either *Herschel* or Hα, yet has $t_{c0}(K_0) \sim 140$ Myr. This cooling time fits remarkably well with the 24 μm estimated L_{TIR}, but the *Herschel* non-detection shows that such a luminosity is not possible (the limit from *Herschel* is $\sim$0.5 dex lower). The BCG is coincident with the X-ray peak, so if it were conforming to the general trend, the cold ICM should be feeding star formation in the galaxy. Further explanation of this BCG requires additional study beyond this current paper.

We now qualitatively compare $L(H\alpha)$ and the total infrared luminosity (Figure 6). We have endeavored to remove inconsistencies in $L(H\alpha)$, such as different aperture sizes and H_0

assumptions (for the older literature measurements). The values are corrected for extinction from our Galaxy, but not for internal reddening, and treatment of the [N II] line is different in the various surveys (see individual papers for more details). Despite these uncertainties and caveats, there appears to be a reasonable correlation ($\sim$0.34 dex scatter; gray solid line) over two orders of magnitude (in L_{TIR}). The four Hα-emitting BCGs undetected by *Herschel* but with $L_{TIR}(24 \mu m)$ lie comfortably on this trend. On closer examination, there appears to be a dichotomy between the highest L_{TIR} sources and the others. Fitting to only BCGs $L_{TIR} < 2 \times 10^{11} L_\odot$, the slope steepens significantly (black solid line) and the scatter decreases to 0.27 dex.

Normal star-forming galaxies typically exhibit extinction $A(H\alpha) \sim 1$ mag (e.g., Kennicutt 1983; Hopkins et al. 2001). For more IR-luminous galaxies ($L_{TIR} > 10^{11} L_\odot$), dust may become increasingly opaque to optical wavelengths and the total SFR tends toward SFR$_{FIR}$ (Calzetti et al. 2010). From the self-consistent relations of Kennicutt (1998),[11] zero extinction (i.e., SFR$_{FIR}$ = SFR(Hα)) would equate to $\log[L(H\alpha)] = \log(L_{TIR}) + 31.34$ (cyan dashed line). The red dash-dotted line in Figure 6 indicates 1 mag of (uncorrected) reddening, which could easily account for the highest luminosity BCGs. However, the best-fit line for the lower luminosity BCGs (black solid) lies well above this relation. The orange dash-dot line indicates SFR(Hα) = SFR$_{FIR}$ − 0.4 mag uncorrected reddening, suggesting that the majority of the low-luminosity sources can be explained by this relatively small extinction or less. The cold gas appears to be less dusty than in normal star-forming galaxies, indicating a different origin for the fuel.

---

[11] SFR$_{FIR}$ $(M_\odot$ yr$^{-1}) = 1.73 \times 10^{-10} L_{TIR}$ $(L_\odot)$; SFR(Hα) $(M_\odot$ yr$^{-1}) = 7.9 \times 10^{-42} L(H\alpha)$ (erg s^{-1}).
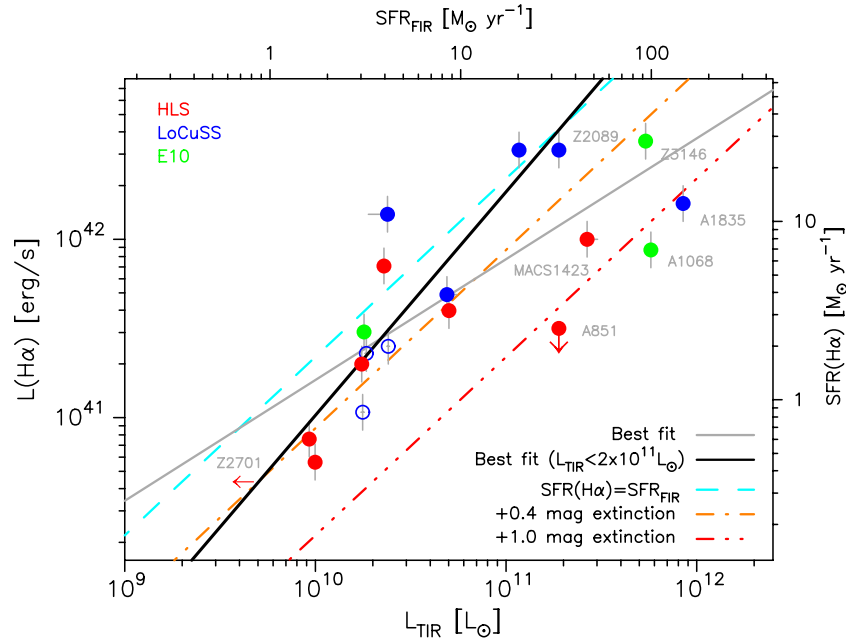
Figure 6. L(Hα) vs. L_{TIR} (from R09 templates) for BCGs included in Table 2. Solid circles are *Herschel* detections; open circles are 24 μm detected only. Colors as in Figure 3. Selected BCGs are labeled (see the text for further details). Gray solid line shows the best fit to all BCGs with detections in both *Herschel* and Hα (rms scatter = 0.34 dex), while the black solid line is the best fit to those $L_{TIR} < 2 \times 10^{11} L_{\odot}$ (scatter = 0.27 dex). The cyan dashed line represents the relation $\log[L(H\alpha)] = \log(L_{TIR}) + 31.34$ (i.e., SFR(Hα) = SFR$_{FIR}$ via Kennicutt 1998). The orange dash-dot and red dash-dotted lines show the same relation, but accounting for 0.4 and 1 mag, respectively, of uncorrected extinction in Hα flux. The corresponding SFRs, via Kennicutt (1998), are also displayed.

(A color version of this figure is available in the online journal.)

It is worth noting that the relation indicating a small apparent extinction could also result from an intrinsically larger Hα flux, e.g., due to an additional heat source (Fabian et al. 2011). For this scenario to be plausible, the effect would need to be more pronounced in the less IR-bright BCGs, which could be true if the absolute contribution to the observed Hα emission was similar in all BCGs and negligible in those with the highest SFRs.

The surprising Hα non-detection of A851 suggests a much higher extinction (A(Hα) $\gtrsim$ 1 mag) than the typical BCG. Further examination of the *HST* optical imaging reveals a large tidal tail, while the BCG also has a projected offset from the X-ray peak of $\sim$280 kpc (Bildfell et al. 2008), 10–20$\times$ greater than the majority of this sample. Even if a cool-core were present it would have little influence. It is likely that galaxy–galaxy interaction (merger or harassment), rather than the cool-core phenomenon, is responsible for the star formation, and hence the extinction resembles the normal star-forming galaxy population.

5.2. Far-infrared Stacking Analysis

We now attempt to constrain the FIR luminosity of "non-cool-core" cluster BCGs. To achieve this, the BCGs in the HLS and LoCuSS sub-samples are classified into three exclusive categories: detected in FIR and Hα, Hα-detected only (i.e., not FIR-detected), and undetected in either FIR or Hα. Note that (1) the three BCGs from E10 would all fall into the first class and (2) we neglect an FIR-detected only category as it would consist of the debatable BCG in A851 alone. For each class, the *Herschel* maps are co-added (stacked) after centering on the optical BCG position and removing exceptionally bright nearby sources via point-source fitting.

Confusion noise is a time-invariant rms uncertainty and hence once reached, integrating longer does not improve the detection limit (in contrast to the more familiar instrument noise).

However, confusion noise is still a zero-averaged Gaussian rms and is not spatially invariant, so stacking on multiple known source positions from a prior catalog can detect a mean flux below the nominal confusion limit (e.g., Marsden et al. 2009). Figure 7 presents the PACS and SPIRE 250 μm stacks for each of three categories. For brevity, we analyze but do not show the longer wavelength SPIRE stacks, which are broadly comparable to 250 μm.

As one would expect, the FIR-detected stacks (11 co-added frames) exhibit a strong source in the center (left panels, Figure 7). This is a useful verification of the stacking algorithm and optical–FIR alignment. The aperture-corrected flux in the stacks equals (to within $\sim$5%) the sum of the individual source fluxes, and the PSF is not significantly larger than the nominal beam size for a single map.

The stack of Hα-detected sources without *Herschel* flux (center panels, Figure 7) only comprises four BCGs (three from shallow LoCuSS maps) and does not significantly improve upon the HLS detection limit. Therefore, although 24 μm photometry indicates that at least three of these sources should be close to the *Herschel* limit for an individual map, the stack does not reveal a detection.

The final category, for those undetected in both Hα and the far-infrared, includes the vast majority of the sample (49 co-added frames; right panels, Figure 7). These can be considered the non-cool-core cluster BCGs. Again, there is no detection, suggesting that a BCG in this class has a mean 3σ upper limit in each band (100–500 μm) of 0.6, 1.1, 1.3, 1.4, 1.8 mJy. These values are well below the confusion limit of a single source in all bands (e.g., from Berta et al. 2010; Nguyen et al. 2010). The dashed line in Figure 3 shows the approximate luminosity limit (as a function of redshift) derived from these *Herschel* flux limits. At any given redshift, the average FIR luminosity of a non-cool-core BCG is at least an order of magnitude below those in cool-core
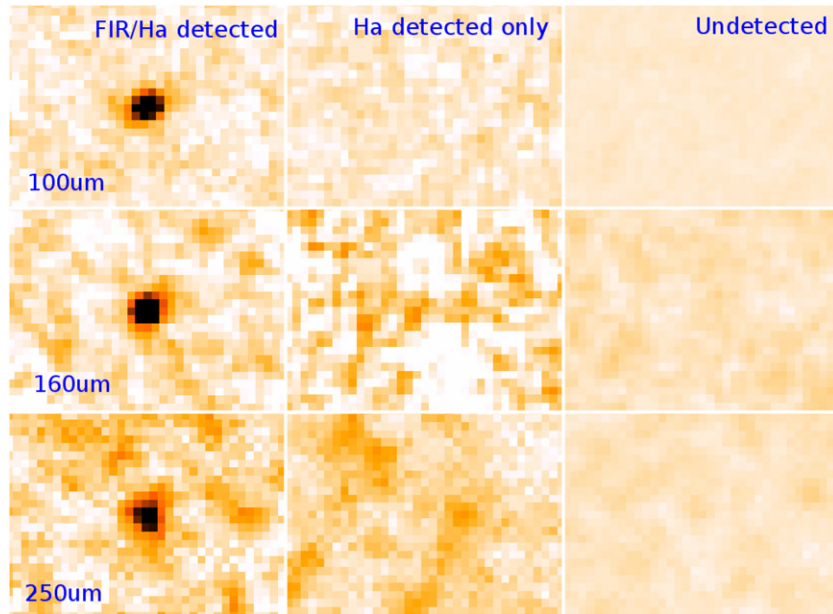
Figure 7. Co-added *Herschel* maps (upper–lower: 100, 160, 250 μm) stacked on optical BCG position for the HLS and LoCuSS subsamples. BCGs are categorized by detections in FIR and Hα emission. Left panels: 11 BCGs with both *Herschel* and Hα detections. Center panels: 4 BCGs detected in Hα, but not by *Herschel*. Right panels: 49 BCGs without FIR or Hα detections. No detection is recovered in the latter two classes, with the undetected (non-cool-core cluster) stack revealing mean 3σ limits of 0.6, 1.1, 1.3, 1.4, 1.8 mJy at 100–500 μm.

(A color version of this figure is available in the online journal.)

clusters, suggesting a mean SFR $< 0.17\ M_\odot$ yr^{-1} at $z \sim 0.2$ and SFR $< 0.42\ M_\odot$ yr^{-1} at $z \sim 0.3$. The stacking analysis supports a bi-modal distribution of far-infrared luminosity, whereby BCGs are either star forming (due to a cooling ICM) or are as quiescent as normal cluster early types.

5.3. Origin of the Dusty Gas

We have presented strong circumstantial evidence that the fuel for star formation in FIR-bright BCGs originates from the cooling ICM. A recent study by Voit & Donahue (2011) asserts that the dusty gas may instead be from normal stellar mass loss, estimating a potential mass contribution up to $8\ M_\odot$ yr^{-1}. We explore this further by calculating the stellar/dust mass ratio for our BCG sample, including limits on the ratio for the population undetected by *Herschel*.

Dust masses are estimated at 500 μm via $T_{\rm dust}$ derived from the blackbody fit, using the formula

$$M_{\rm dust} = \frac{4\pi D^2 f_{500}}{\kappa_{\rm abs} 4\pi B_\lambda(T_{\rm dust})}, \qquad (3)$$

where f_{500} is the rest frame 500 μm flux, B_λ is the Planck function, and $\kappa_{\rm abs} = 0.95$ cm^2 g^{-1} is the absorption coefficient at 500 μm (Draine 2003). Rest frame 500 μm flux is estimated from the best-fit R09 template. We derive stellar luminosity from the 2MASS total K-band magnitude, adjusted for galactic extinction and K-correction. The redshift-dependent conversion from K-band luminosity to stellar mass follows the formulation presented in Arnouts et al. (2007).[12]

The *Herschel*-detected BCGs have $200 < M_*/M_{\rm dust} < 6000$ with a mean $M_*/M_{\rm dust} = 1570$ (Figure 8). The limits for individual non-detected LoCuSS BCGs are inconclusive as the *Herschel* imaging is fairly shallow, while those from HLS imaging have limits on $M_*/M_{\rm dust}$ of 4000–10000. Given that

---

[12] $\log({\rm M}/{\rm L}_K) = (-0.27 \pm 0.03)z - (0.05 \pm 0.03)$.
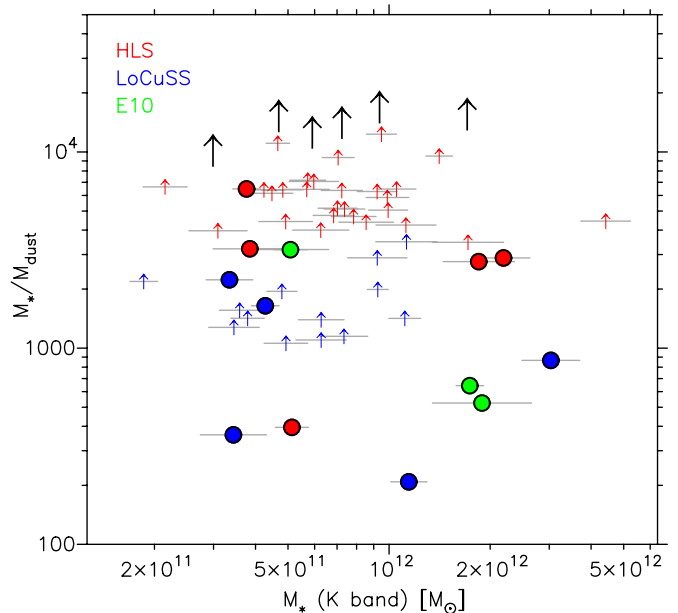

Figure 8. Ratio of stellar mass to dust mass, $M_*/M_{\rm dust}$, vs. the stellar mass. Circular symbols represent *Herschel*-detected BCGs. Lower limits for Hershel non-detections are given by small colored arrows (colors indicate sample as in previous plots; note HLS galaxies are better constrained as the limits on FIR flux, and hence dust mass, are lower). When FIR-undetected BCGs are stacked within bins of similar stellar mass, the limits in $M_*/M_{\rm dust}$ can be raised to the larger black arrows (any stack of individually undetected BCGs gives a non-detection; Figure 7).

(A color version of this figure is available in the online journal.)

the entire stack of FIR-undetected BCGs shows no *Herschel* flux (Figure 7), we can bin the undetected BCGs by stellar mass (choosing six bins with seven BCGs each) and estimate the limit on $M_*/M_{\rm dust}$ for the stack. The limit for each stellar mass bin is very similar with a mean $M_*/M_{\rm dust} > 15000$ or an
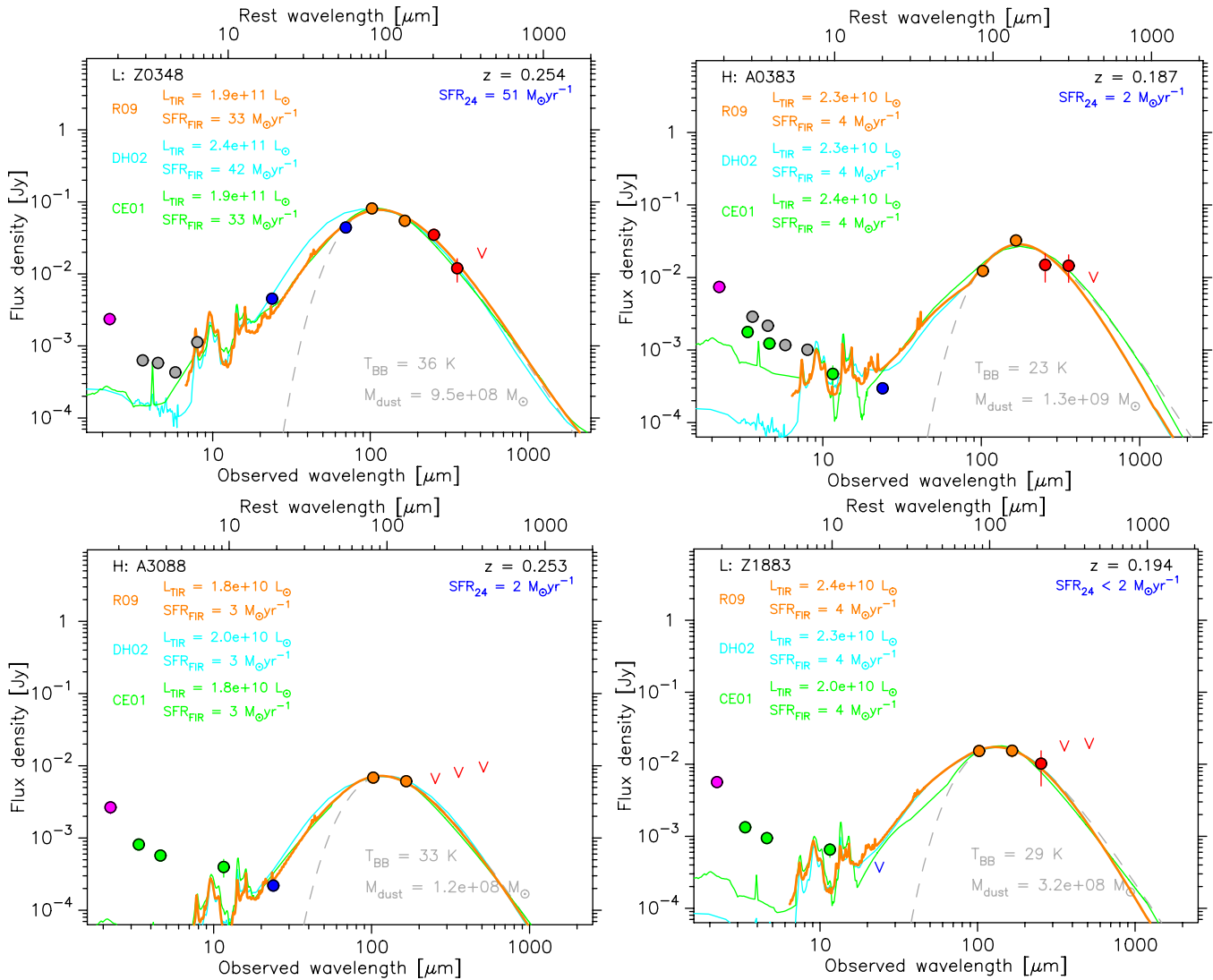
Figure 9. Far-infrared SEDs for *Herschel*-detected BCGs (sample, name, and redshift shown in black). PACS and SPIRE detections displayed as orange and red circles, respectively. Upper limits are shown as "v" at the 3σ detection limit. Additional photometry is also displayed: 2MASS *K* band (magenta); *Spitzer* IRAC (gray) and MIPS (blue); *WISE* (green); *IRAS* (cyan); SCUBA (black). A modified-blackbody is fit to the *Herschel* points (dashed line), with the temperature and estimated dust mass shown in the lower-right corner. Best-fit templates from three libraries are also plotted: orange, Rieke et al. (2009); cyan, Dale & Helou (2002); and green, Chary & Elbaz (2001). Derived L_{TIR} and SFR$_{FIR}$ for each are given in matching colors. MIPS 24 μm derived SFR is shown in blue in the upper-right corner.
(A color version of this figure is available in the online journal.)

order of magnitude higher than the ratio for *Herschel*-detected BCGs of the same stellar mass. If stellar mass loss were the dominant origin for the dusty gas driving BCG star formation, we would expect all BCGs of a given stellar mass to show similar SFRs. Otherwise, there would still be a need for a mechanism to trigger star formation in some BCGs while leaving the majority quiescent. We demonstrate a very good relation between SFR and central cooling time in Figure 5, indicating a much stronger probability that the star formation is driven and fueled by the cooling ICM.

6. SUMMARY

We present analysis of the largest cluster sample observed with at least five *Herschel* band (100–500 μm), combining the HLS and LoCuSS data sets. In total, the sample comprises 68 BCGs $0.08 < z < 1.0$, of which 15 ($22^{+6.2}_{-5.3}\%$) are detected by *Herschel*, equivalent to $L_{TIR} > 10^{10} L_\odot$ (SFR $\gtrsim 2 M_\odot$ yr^{-1}), including 7 classified as LIRGs. This fractional detection rate

is similar to the LoCuSS clusters alone ($25^{+10.0}_{-8.2}\%$), which can be considered statistically identical to a volume-limited X-ray-luminosity-selected sample. Eighteen of the 68 BCGs ($26^{+6.4}_{-5.7}\%$) have detected Hα line emission. Generally, far-infrared and Hα detections correspond well with 24 μm based extrapolations to the far-infrared suggesting that most Hα-detected BCGs unseen by *Herschel* are only just below the detection limit.

We present four associated strands of circumstantial evidence which strongly suggest that the fuel for star formation in FIR-bright BCGs is not the same as in normal star-forming galaxies, but is directly connected to the central gas cooling in the cluster core.

1. A very good anti-correlation between *Herschel*-derived SFR and the X-ray cooling time, for BCGs in cool-core clusters ($t_{c0}(K_0) \lesssim 1$ Gyr).
2. FIR stacks of the *Herschel*-undetected BCGs (49 sources) show no discernible flux, placing mean 3σ upper limits of 0.6, 1.1, 1.3, 1.4, 1.8 mJy on the five bands (100–500 μm)
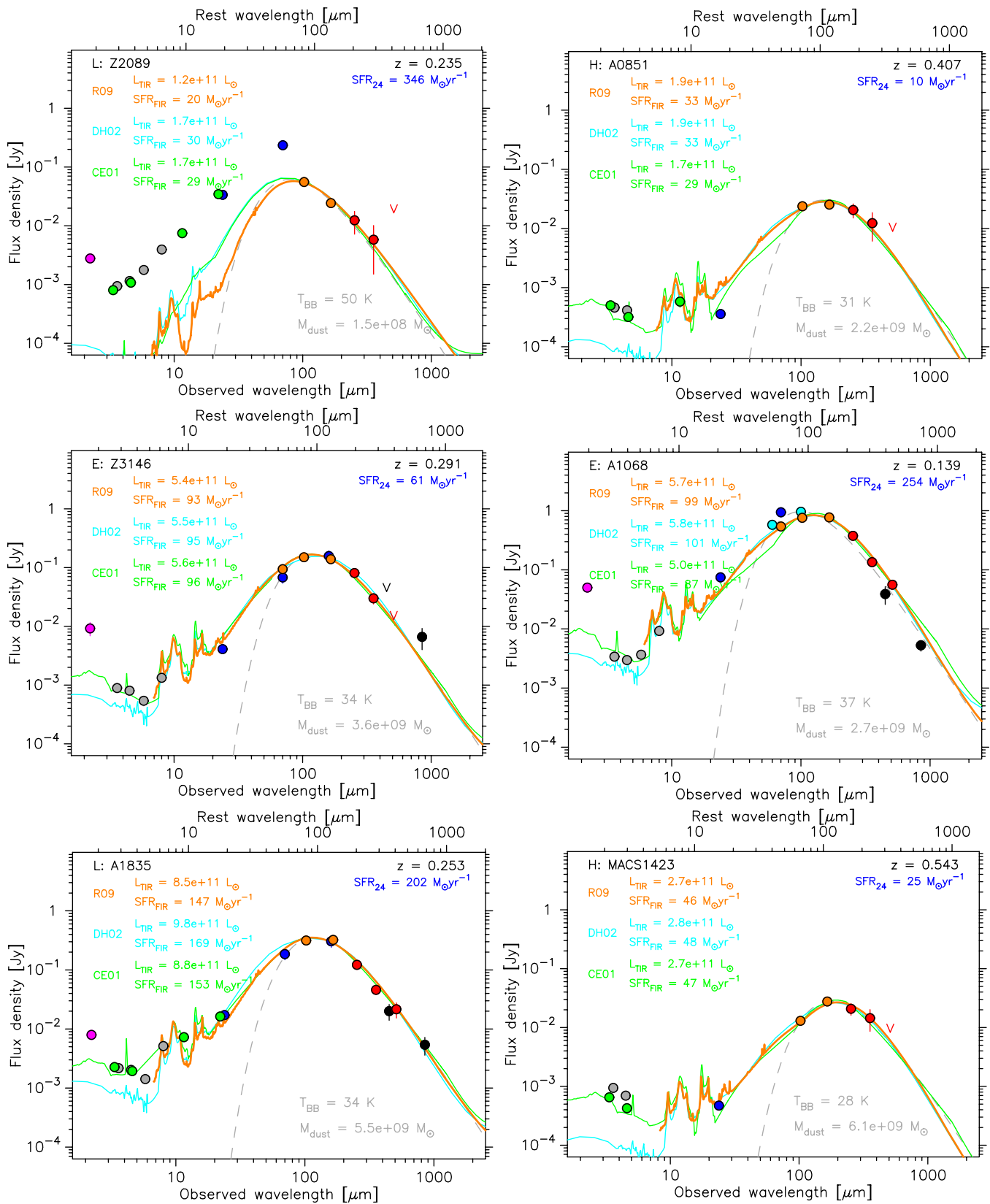
Figure 10. Far-infrared SEDs for *Herschel*-detected BCGs. Layout as in Figure 9.
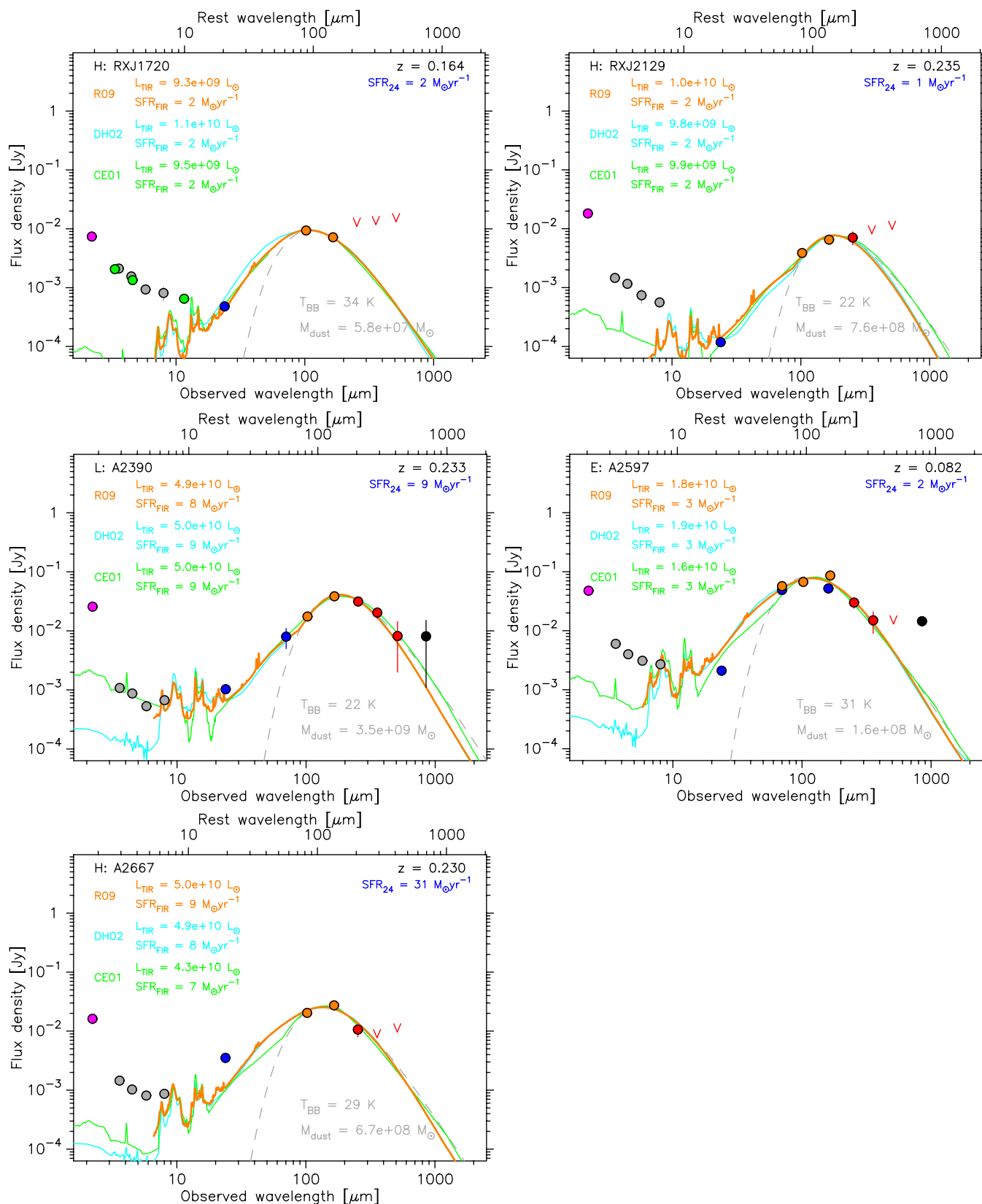(A color version of this figure is available in the online journal.)

Figure 11. Far-infrared SEDs for *Herschel*-detected BCGs. Layout as in Figure 9.

(A color version of this figure is available in the online journal.)

and implying a mean SFR for non-cool-core cluster BCGs of SFR $\ll 1$ $M_\odot$ yr^{-1} ($z < 0.4$).

3. A surprisingly low Hα extinction ($\sim$0.4 mag) for all but the most IR-luminous, *Herschel*-detected BCGs ($L_{\mathrm{TIR}} < 2 \times 10^{11}$ $L_\odot$) compared to similar normal star-forming galaxies ($\sim$1 mag, e.g., Kennicutt 1983) implying that the gas is significantly less dusty.

4. The stellar-to-dust mass ratio of *Herschel*-detected BCGs is at least an order of magnitude below the ratio for non-cool-core BCGs of the same stellar mass suggesting that normal stellar mass loss is unlikely to be the dominant star formation fuel source.

We find no significant evolution in BCG dust properties with redshift, as previously reported in the Hα observations of Crawford et al. (1999) and recently shown for all star-forming galaxies in large survey volumes (e.g., Hwang et al. 2010). However, we note that our BCG sample is not ideally distributed in redshift space for such an analysis. Despite the difference in Hα extinction, the FIR dust properties of BCGs explored briefly in this study (e.g., characteristic temperature) are indistinguishable from the IR-bright population as a whole.

APPENDIX

INFRARED SED FITS

Figures 9–11 present the infrared (observed frame $\lambda = 2$–2000 μm) SED for the 15 *Herschel*-detected BCGs in HLS, LoCuSS, and E10.

REFERENCES

Adelman-McCarthy, J. K., Agüeros, M. A., Allam, S. S., et al. 2008, ApJS, 175, 297
Arnouts, S., Walcher, C. J., Le Fèvre, O., et al. 2007, A&A, 476, 137
Berta, S., Magnelli, B., Lutz, D., et al. 2010, A&A, 518, L30
Bertin, E., & Arnouts, S. 1996, A&A, 117, 393
Bildfell, C., Hoekstra, H., Babul, A., et al. 2008, MNRAS, 389, 1637
Blain, A. W., Barnard, V. E., & Chapman, S. C. 2003, MNRAS, 338, 733
Böhringer, H., Voges, W., Fabian, A. C., Edge, A. C., & Neumann, D. M. 1993, MNRAS, 264, 25
Bower, R. G., Benson, A. J., Malbon, R., et al. 2006, MNRAS, 370, 645
Calzetti, D., Wu, S.-Y., Hong, S., et al. 2010, ApJ, 714, 1256
Cavagnolo, K. W., Donahue, M., Voit, G. M., & Sun, M. 2008, ApJ, 683, 107
Cavagnolo, K. W., Donahue, M., Voit, G. M., & Sun, M. 2009, ApJS, 182, 12
Chary, R., & Elbaz, D. 2001, ApJ, 556, 562
Conselice, C. S., Gallagher, J. S., & Wyse, R. F. G. 2001, AJ, 122, 2281
Cowie, L. L., & Binney, J. 1977, ApJ, 215, 723
Crawford, C. S., Allen, S. W., Ebeling, H., Edge, A. C., & Fabian, A. C. 1999, MNRAS, 306, 857
Crawford, C. S., Hatch, N. A., Fabian, A. C., & Sanders, J. S. 2005, MNRAS, 363, 216
Dale, D. A., & Helou, G. 2002, ApJ, 576, 159
David, L. P., & Kempner, J. 2004, ApJ, 613, 831
Donahue, M., de Messières, G. E., O'Connell, R. W., et al. 2011, ApJ, 732, 40
Donahue, M., Stocke, J. T., & Gioia, I. M. 1992, ApJ, 385, 49
Donahue, M., Voit, G. M., O'Dea, C. P., Baum, S. A., & Sparks, W. B. 2005, ApJ, 630, L13
Draine, B. T. 2003, ARA&A, 41, 241
Edge, A. C. 2001, MNRAS, 328, 762
Edge, A. C., Stewart, G. C., & Fabian, A. C. 1992, MNRAS, 258, 177
Edge, A. C., Oonk, J. B. R., Mittal, R., et al. 2010a, A&A, 518, L46
Edge, A. C., Oonk, J. B. R., Mittal, R., et al. 2010b, A&A, 518, L47 (E10)
Edge, A. C., Wilman, R. J., Johnstone, R. M., et al. 2002, MNRAS, 337, 49
Egami, E., Misselt, K. A., Rieke, G. H., et al. 2006a, ApJ, 647, 922
Egami, E., Rex, M., Rawle, T. D., et al. 2010, A&A, 518, L12
Egami, E., Rieke, G. H., Fadda, D., & Hines, D. C. 2006b, ApJ, 652, L21
Fabian, A. C., & Nulsen, P. E. J. 1977, MNRAS, 180, 479
Fabian, A. C., Sanders, J. S., Williams, R. J. R., et al. 2011, MNRAS, 417, 172
Griffin, M., Abergel, A., Abreu, A., et al. 2010, A&A, 518, L3
Haines, C. P., Smith, G. P., Egami, E., et al. 2009, ApJ, 704, 126
Hopkins, A. M., Connolly, A. J., Haarsma, D. B., et al. 2001, AJ, 122, 288
Hudson, D. S., Mittal, R., Reiprich, T. H., et al. 2010, A&A, 513, 37
Hwang, H. S., Elbaz, D., Magdis, G., et al. 2010, MNRAS, 409, 75
Johnstone, R. M., Hatch, N. A., Ferland, G. J., et al. 2007, MNRAS, 382, 1246
Kennicutt, R. C., Jr. 1983, ApJ, 272, 54
Kennicutt, R. C., Jr. 1998, ARA&A, 36, 189
Marsden, G., Ade, P. A. R., Bock, J. J., et al. 2009, ApJ, 707, 1729
McDonald, M., Veilleux, S., & Mushotzky, R. 2011, ApJ, 731, 33
McNamara, B. R., & Nulsen, P. E. J. 2007, ARA&A, 45, 117
McNamara, B. R., Wise, M., Nulsen, P. E. J., et al. 2000, ApJ, 534, 135
Mittal, R., O'Dea, C. P., Ferland, G., et al. 2011, MNRAS, 418, 2386
Nguyen, H. T., Schulz, B., Levenson, L., et al. 2010, A&A, 518, L5
O'Dea, C. P., Baum, S. A., Privon, G., et al. 2008, ApJ, 681, 1035
Okabe, N., Takada, M., Umetsu, K., Futamase, T., & Smith, G. P. 2010, PASJ, 62, 811
Ott, S. 2010, in ASP Conf. Ser. 434, Astronomical Data Analysis Software and Systems XIX, ed. Y. Mizumoto, K.-I. Morita, & M. Ohishi (San Francisco, CA: ASP), 139
Peterson, J. R., & Fabian, A. C. 2006, Phys. Rep., 427, 1
Pilbratt, G., Riedinger, J. R., Passvogel, T., et al. 2010, A&A, 518, L1
Poglitsch, A., Waelkens, C., Geis, N., et al. 2010, A&A, 518, L2
Quillen, A. C., Zufelt, N., Park, J., et al. 2008, ApJS, 176, 39
Rawle, T. D., Chung, S. M., Fadda, D., et al. 2010, A&A, 518, L14
Rex, M., Rawle, T. D., Egami, E., et al. 2010, A&A, 518, L13
Rieke, G. H., Alonso-Herrero, A., Weiner, B. J., et al. 2009, ApJ, 692, 556 (R09)
Salomé, P., & Combes, F. 2003, A&A, 412, 657
Silk, J., & Rees, M. J. 1998, A&A, 331, 1
Skrutskie, M. F., Cutri, R. M., Stiening, R., et al. 2006, AJ, 131, 1163
Smith, G., Haines, C. P., Pereira, M. J., et al. 2010, A&A, 518, L18
Tamura, T., Kaastra, J. S., Peterson, J. R., et al. 2001, A&A, 365, L87
Voit, G. M., & Donahue, M. 2011, ApJ, 738, L24
Wright, E. L., Eisenhardt, P. R. M., Mainzer, A. K., et al. 2010, AJ, 140, 1868